ACS APPLIED MATERIALS & INTERFACES

Research Article

www.acsami.org

Phase-Shifted PFH@PLGA/Fe_3O_4 Nanocapsules for MRI/US Imaging and Photothermal Therapy with near-Infrared Irradiation

Yajing Zhao,[†] Weixiang Song,[†] Dong Wang,[‡] Haitao Ran,[†] Ronghui Wang,[†] Yuanzhi Yao,[†] Zhigang Wang,[†] Yuanyi Zheng,*[,†] and Pan Li*[,†]

[†]Second Affiliated Hospital, Institute of Ultrasound Imaging, Chongqing Medical University, Chongqing 400010, P.R. China

[‡]Department of Ultrasound, Ministry of Education Key Laboratory of Child Development and Disorders, Children's Hospital of Chongqing Medical University, Chongqing 400014, P.R. China

Supporting Information

ABSTRACT: Photothermal therapy (PTT) utilizes photothermal conversion reagents to generate heat energy from absorbed light to effectively treat various malignant diseases. This approach has attracted broad and increasing interest in cancer treatment. Near-infrared (NIR)-induced PTT is particularly attractive because of its minimal absorbance by normal tissue and relatively deep tissue penetration. To improve the efficacy of PTT, we have developed nanocapsules encapsulating superparamagnetic iron oxide (Fe_3O_4) as synergistic agents for NIR-induced PTT. In this study, phase-shift and NIR photoabsorbing poly(lactic-*co*-glycolic acid) (PLGA) nanocapsules (perfluorohexane (PFH)@PLGA/Fe_3O_4) were fabricated for MRI/US dual-modal imaging-guided PTT. The multifunctional nanocapsules can be used not only to increase the local tumor temperature by absorbing the NIR energy but also as bimodal contrast agents for both MRI and US imaging. Such nanocapsules can be converted into microbubbles under NIR irradiation, which produces excellent contrast for US imaging and enhanced cancer ablation. We refer to the nanocapsule phase transition process induced by the infrared lamp as NIR radiation droplet vaporization (NIRDV).

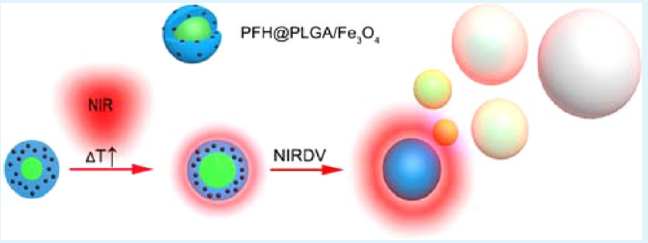

KEYWORDS: *near-infrared, phase-shift, photothermal therapy*

1. INTRODUCTION

New and effective hyperthermia treatments for cancer have recently become topics of intensive research interest. The combination of nanomaterials with high optical absorption and near-infrared (NIR) irradiation is an important method of photothermal therapy (PTT).[1−6] With the application of a photoabsorbing agent, tremendous amounts of NIR light are absorbed and converted into heat for the specific ablation of cancer cells. NIR light can penetrate deeply into tissues without causing extensive damage to the surrounding normal tissue and has the potential for treating tumors in cases where surgical resection is not feasible. The ability of various nanomaterials with high optical absorbance, such as silica nanospheres,[2,7] gold nanoshells,[2,6,8,9] a $Cu_{2-x}S$ shell,[10] graphene oxide,[4] and Fe_3O_4 nanoparticles,[1,11−13] to increase local temperatures has been examined. These photoabsorbers have been demonstrated to efficiently absorb NIR light and actively generate heat in local tumor tissues in a number of studies. Furthermore, these nanoparticles can simultaneously serve as contrast agents for MRI, US or CT imaging, which are preferred methods for accurate cancer diagnosis and for locating the tumor site to guide the external NIR-induced photothermal ablation of tumors.[14] MRI has great advantages in identifying the accurate location and size of tumors prior to NIR-induced PTT because of its excellent spatial and anatomical resolution, nonionizing radiation, and high sensitivity. US imaging can be used to monitor the treatment procedure in real time because of its unique features of real-time imaging, low cost, high safety, and ready availability for portable devices. The integration of MRI and US contrast imaging provides excellent diagnosis modality for imaging guided and monitored photothermal tumor ablation.[15,16]

Fe_3O_4 nanoparticles can be used as NIR photoabsorbers as well as magnetic contrast agents, leading to NIR PTT and MR imaging for efficient tumor ablation.[1,12,17,18] Chu et al. reported that Fe_3O_4 nanoparticles of various shapes can exhibit strong photothermal effects during red and NIR laser irradiation.[11] Shi et al. reported that magnetic Fe_3O_4 nanoparticles are utilized as versatile probes in biomedical applications because of their utility in MR imaging.[6] However, Fe_3O_4 nanoparticles cannot be used as an efficient ultrasound contrast agent without acoustic impedance mismatch usually generated by perfluorocarbon (PFC) gas. The nanometric size of nanoparticles offers good stability of circulation and other benefits, such as an EPR effect, in tumor tissue but also limits the space available for loading PFCs. Ultrasound microbubbles encapsulating PFCs

Received: March 2, 2015
Accepted: June 11, 2015
Published: June 11, 2015

DOI: 10.1021/acsami.5b01873
ACS Appl. Mater. Interfaces 2015, 7, 14231−14242

Scheme 1. Schematic of the Structure of PFH@PLGA/Fe_3O_4 Nanocapsules and a Schematic of the Phase-Transition Process by the Method of near-Infrared Radiation Droplet Vaporization (NIRDV)

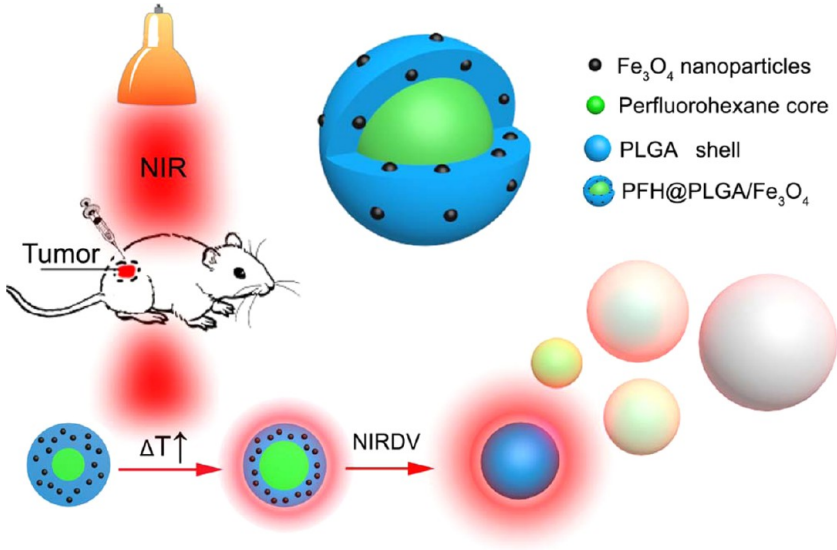

produce excellent contrast ultrasound imaging, but has shortcomings such as short circulation times, low payloads, and poor extravasation into tumor tissue. These problems could be solved by developing phase-shift Fe_3O_4 nanoparticles encapsulating liquid perfluorocarbon, which can be transformed into microbubbles after vaporization by ultrasound or laser.[19,20]

Nanocapsules encapsulating PFC liquid droplets can be vaporized into gas bubbles by acoustic or optical activation; these processes are known as the acoustic droplet vaporization (ADV) and optical droplet vaporization (ODV) techniques, respectively.[21] ADV and ODV techniques have been used in tumor therapy and imaging in a number of studies.[5,22−24] The thermoelastic expansion of phase-shift nanoemulsions has been reported to enhance local tumor thermal ablation effects without significantly increasing the temperature. For instance, several groups have reported that ADV can greatly improve the clinical efficacy of high-intensity focused ultrasound thermal ablation therapy.[25−28] Additionally, the phase-shift nanocapsules can be used for contrast-enhanced ultrasound imaging by the highly echogenic microbubbles.[29−31] Xu et al. demonstrated that heat-sensitive microbubbles (HSM) can be used as accurate ultrasound contrast agents for intraoperative assessment of ablation margins in cancer thermal ablation therapies.[32] Kripfgans et al. employed phase-shift nanocapsules for both occlusion therapy and diagnosis using the ADV method.[22]

Hence, combining nanomaterials that exhibit both high optical absorbance and phase-shift properties might significantly improve the NIR-induced PTT effect. In this study, we designed temperature-sensitive and NIR photoabsorption polymeric nanocapsules (perfluorohexane (PFH)@PLGA/Fe_3O_4), which can not only be used to increase the local tumor temperature by absorbing NIR energy, but are also capable of enhancing tumor therapy via a phase-shift thermoelastic expansion effect. Furthermore, they can also be used as a US/MRI dual-modal contrast agent for imaging-guided therapy. Scheme 1 shows a schematic of the structure of PFH@PLGA/Fe_3O_4 nanocapsules and a schematic of the phase-transition process. The PFH@PLGA/Fe_3O_4 nanocapsules consist of three representative parts: (1) an organic polymer shell composed of poly(lactic-*co*-glycolic acid) (PLGA); (2) the light-absorbing substance (magnetic Fe_3O_4 nanoparticles) embedded in the shell; and (3) a liquid core composed of temperature-sensitive PFH.

Liquid PFH is a typical phase-shift material that can be converted into gas when the temperature approaches its boiling point. PFH is often encapsulated in nanocapsules and is extensively used as a synergistic and ultrasound contrast agent for tumor therapy and ultrasound imaging.[26,28] The elaborately designed temperature-sensitive nanocapsules (PFH@PLGA/Fe_3O_4) can be transformed from liquid into gas after being exposed to high temperatures and/or infrared radiation. Upon exposure to infrared radiation, the magnetic Fe_3O_4 nanoparticles encapsulated in the PFH@PLGA/Fe_3O_4 nanocapsule shells absorb the infrared light and transform this light energy into heat energy, thereby facilitating vaporization of the PFH inner liquid. We named this phase-transition process NIR radiation droplet vaporization (NIRDV). Because of the phase transformation, such vaporization enables the nanosized emulsions to generate large numbers of micron-sized bubbles via the phase-transition process from liquid to gas. The heat energy generated and the thermoelastic expansion caused by the nanocapsule phase transition can synergistically enhance the effect of thermal ablation on local tumors. Moreover, the existence of Fe_3O_4 and the microbubbles generated using the phase-transition process give the PFH@PLGA/Fe_3O_4 nanocapsules magnetic resonance and can be used as an ultrasound contrast agent, thus achieving MR/US-guided tumor therapy.

In this study, we first fabricated phase-shift PFH@PLGA/Fe_3O_4 nanocapsules and demonstrated the NIRDV process for imaging guided PTT. We then tested whether the PFH@PLGA/Fe_3O_4 nanocapsules could serve both as synergistic agents to strengthen tumor ablation efficiency and as contrast agents to provide significant contrast enhancement in MR and US imaging via the NIRDV method.

2. EXPERIMENTAL SECTION

2.1. Materials. Poly(lactic-*co*-glycolic acid) (PLGA) (lactide:glycolide =50:50, MW = 12 000 Da) was purchased from the Shan-dong Key Laboratory of Medical Polymer Materials(Shan-dong, China).

DOI: 10.1021/acsami.5b01873
ACS Appl. Mater. Interfaces 2015, 7, 14231−14242

Oleic-acid-coated Fe_3O_4 nanoparticles (d = 10 nm) were purchased from Ocean Nano Tech, Inc. (Arkansas, USA). PFH was purchased from Alfa Aesar (U.K.). Poly(vinyl alcohol) (PVA, 99% MW = 30 000−70 000 Da) was obtained from Sigma-Aldrich (USA). All chemicals used in this work were of analytical grade and were used as received.

2.2. Preparation of Nanocapsules. PLGA nanocapsules encapsulating Fe_3O_4 and PFH (PFH@PLGA/Fe_3O_4) were fabricated using a new modified emulsion evaporation process. In a typical procedure, 15 mg of solid and nanosized Fe_3O_4 particles was added to a solution of 2 mL of $CHCl_3$ and 100 mg of PLGA. Subsequently, 0.8 mL of liquid PFH was added to the mixture, which was then oscillated slightly. The solution was poured into 10 mL of cold PVA solution (5% w/v) and emulsified in an ice bath using an ultrasonic probe (SONICS & MATERIALS, Inc., USA) at 50% energy for 6 min. In addition, a 20 mL isopropanol solution (2% v/v) was added to the aforementioned emulsion to stabilize the nanocapsules. The final emulsion was then mechanically mixed for 2 h to extract $CHCl_3$. Subsequently, the solution was centrifuged at 7500 rpm for 5 min, the supernatant was discarded, and the precipitate was washed with deionized water. The process of washing and centrifugation was repeated three times. Finally, the nanocapsules were collected and stored at 4 °C for further use. The blank PLGA nanocapsules, PLGA nanocapsules encapsulating PFH (PFH@PLGA), and PLGA nanocapsules encapsulating Fe_3O_4 (Fe_3O_4@PLGA) were fabricated and used as control groups.

2.3. Structural Characterization of Nanocapsules. The PFH@PLGA/Fe_3O_4 nanocapsules were observed by scanning electron microscopy (SEM, Hitachi S-3400N, Japan). To confirm the presence of Fe_3O_4 nanoparticles in nanocapsule shells, the structures of the blank PLGA, Fe_3O_4@PLGA and PFH@PLGA/Fe_3O_4 nanocapsules were analyzed by transmission electron microscopy (TEM, Hitachi H-7600, Japan). The size distribution and zeta potential of the PFH@PLGA/Fe_3O_4 nanocapsules were determined using a Malvern Zetasizer Nano ZS unit (Malvern Instruments, UK). The amount of Fe_3O_4 nanoparticles encapsulated in the nanocapsules with different iron concentrations (2.5, 5, 10, 20, 40, 80, 160, 320, 640, and 1280 μg/mL) was measured using an atomic absorption spectrometry method. UV−vis-NIR absorption spectrum of PFH@PLGA/Fe_3O_4 was performed on UV−vis−-NIR spectrophotometer (Lambda 950, PerkinElmer, USA) at room temperature.

2.4. Cell Culture and Animal Experiments. Ovarian cancer cell line $SKOV_3$ was obtained from the Chongqing Key Laboratory of Ultrasound Molecular Imaging of Chongqing Medical University. Cells were cultured in RPMI-1640 medium supplemented with 10% fetal bovine serum (FBS) at 37 °C for cell experiments and establishment of the tumor model. Female nude mice (4−6 weeks; weight, 18−22 g) were purchased from and bred at the Experimental Animal Center of Chongqing Medical University. All animal experiments were approved by the Animal Ethics Committee at Chongqing Medical University. To establish the animal tumor model, we inoculated 60 4- to 6-week-old female nude mice subcutaneously in the right flank with $SKOV_3$ cells suspended in serum-free RPMI-1640 medium (1×10^6 cells/100 μL/nude mice). The US imaging in vivo and the photothermal destruction of the tumors were initiated one month after the tumor inoculation, when the tumors reached a size of 7−10 mm.

2.5. In Vitro and in Vivo MRI Assessment of PFH@PLGA/Fe_3O_4 Nanocapsules. Deionized water (I), pure nanocapsules (II), and PFH@PLGA/Fe_3O_4 nanocapsules with different iron concentrations (III, 2.5 μg/mL; IV, 5 μg/mL; V, 10 μg/mL; VI, 20 μg/mL; VII, 40 μg/mL; VIII, 80 μg/mL; IX, 160 μg/mL; X, 320 μg/mL; XI, 640 μg/mL; XII, 1280 μg/mL) were placed in Eppendorf tubes 1 cm in diameter and imaged on a Philips Achieva 3.0 T MRI scanner (Philips Healthcare, Andover, MA). The imaging parameters for the T2*-weighted (T2*WI) gradient-echo were set as follows: Fast field echo (FFE), TR = 30.2 ms, TE = 9.2 ms, flip = 45°, FOV = 180 mm, and slice thickness = 3.0 mm. The MRI signal intensity (SI) within the region of interest (ROI) was measured.

PFH@PLGA/Fe_3O_4 nanocapsules (320 μg/mL, 0.2 mL) were injected into the tail veins of nude mice at a dose of 1 mL/kg. Besides, some other nude mice received a percutaneous injection of PFH@PLGA/Fe_3O_4 nanocapsule solutions into the site of the tumor. T2*-weighted images were acquired before after injection. To acquire the T2*-weighted images, we ran turbo spin echo (TSE) sequences at TR values of 3603.37 ms, TE = 80 ms, flip = 90, FOV = 160 mm, and slice thickness =4.0 mm. The SI was determined by comparing SI pre- and post-ROI in the liver parenchyma and tumor tissue.

2.6. NIR-Induced Phase Transition for US Imaging with PFH@PLGA/Fe_3O_4 Nanocapsules. Approximately 1 mL of the PFH@PLGA/Fe_3O_4 nanocapsule suspension was injected into a transparent rubber tube (with a diameter of 2 mm) via syringe. The tube filled with nanocapsules was then irradiated with portable infrared therapy apparatus (Warren HongliHLH-1, Chongqing, China) with wavelength coverage of 0.78−2.8 μm (1.5 W/cm^2). An infrared thermometer (Fluke Ti32; USA) was used to monitor the temperature of the nanocapsules in the rubber tube. The phase transition of the nanocapsules was observed under the optical microscope. In addition, ultrasonography was performed before NIR irradiation and when the temperature of the nanocapsules increased to 40, 50 °, and 60 °C after irradiation.

One month after the tumor inoculation, nude mice bearing xenograft tumors were used to investigate the enhancement effect of nanocapsules for contrast US imaging after NIR infrared irradiation. Twenty-four nude mice with xenograft tumors were divided into four groups: (I) PLGA combined with infrared irradiation, (II) PFH@PLGA combined with infrared irradiation, (III) Fe_3O_4@PLGA combined with infrared irradiation and (IV) PFH@PLGA/Fe_3O_4 combined with infrared irradiation. In the four groups, nude mice received a percutaneous injection of 0.2 mL (320 μg/mL) of PLGA, PFH@PLGA, Fe_3O_4@PLGA, and PFH@PLGA/Fe_3O_4 nanocapsule solutions at the tumor sites and were massaged for 1 min before receiving infrared irradiation. Afterward, all mice were exposed to infrared irradiation. To monitor the temperature of the tumor tissue during irradiation, we inserted the probe of the thermocouple thermometer (FLE5008, Hangzhou, China) into the tumor tissue. Ultrasonography was performed at tumor sites in all mice before NIR irradiation and at 2, 5, and 12 min after irradiation. The corresponding contrast ultrasound images were recorded.

2.7. NIR-Induced Photothermal Effect on Cell Ablation in Vitro. *2.7.1. NIR-Induced Phase Transition of PFH@PLGA/Fe_3O_4 Nanocapsules in Cells.* Cells were dyed with DIO for 30 min and then washed three times with PBS. The ovarian cancer $SKOV_3$ cells were then incubated with PFH@PLGA/Fe_3O_4 nanocapsules labeled by Dil for 3 h in a standard cell culture dish. The cells were subsequently washed three times with PBS. A fluorescence inverted microscope (Olympus IX53; Canada) was used to observe the cells and nanocapsules. The cells were then subjected to infrared irradiation, and the fluorescence inverted microscope was used to observe the progress of the phase transition of nanocapsules assembling around or inside the cells.

2.7.2. Cell Apoptosis Induced by NIR with PFH@PLGA/Fe_3O_4 Nanocapsules. During the logarithmic phase, ovarian cancer cells were seeded in 10 cm culture dishes at a density of 7×10^6 cells per dish. After 24 h incubation, we assigned the dishes randomly into groups, with each group consisting of six samples. To confirm the effect of the infrared ray distance on cell apoptosis, we set up eight groups (groups 1−8). First, 0.2 mL (320 μg/mL) PFH@PLGA/Fe_3O_4 nanocapsules were added to the culture media of seven groups (groups 1−7) and incubated for 3 h. Groups 1−6 were irradiated for 6 min at different infrared irradiation distances (group 1, 3 cm; group 2, 6 cm; group 3, 9 cm; group 4, 12 cm; group 5, 15 cm; and group 6, 18 cm). Groups 7 and 8 were the control groups that were not irradiated. Then, the cells were continuously cultured overnight after irradiation. The cells were digested with trypsin and centrifuged the next day, and flow cytometry was performed to analyze cell apoptosis in each group. On the basis of the results, we selected an appropriate irradiation distance for the subsequent experiments.

DOI: 10.1021/acsami.5b01873
ACS Appl. Mater. Interfaces 2015, 7, 14231−14242

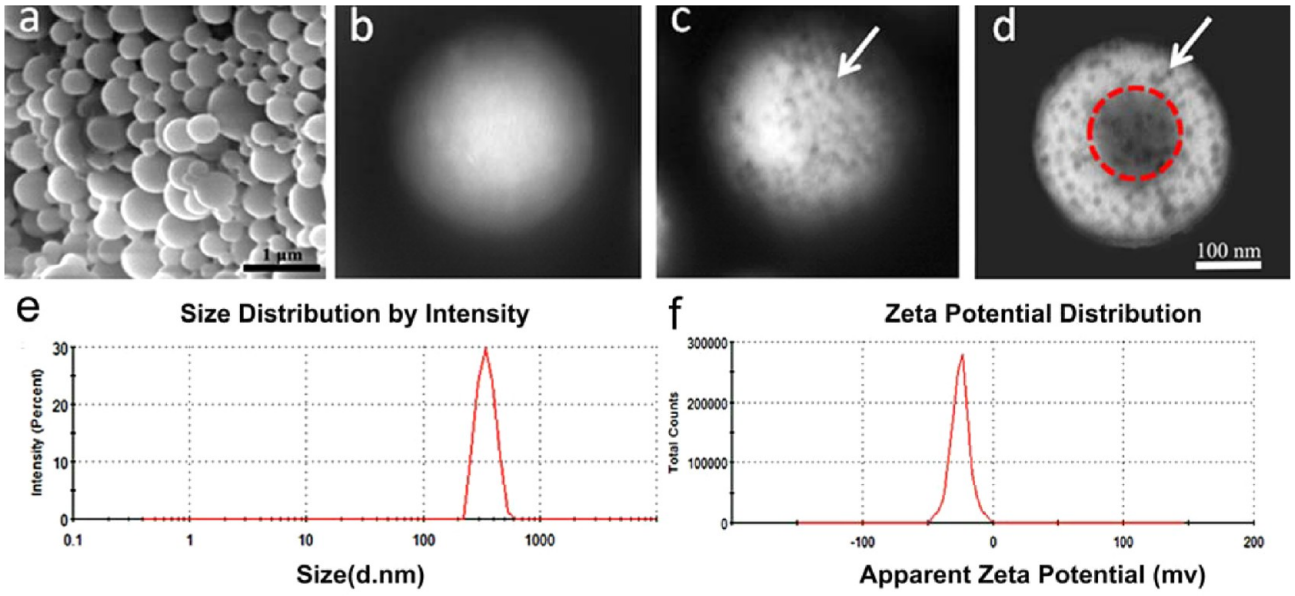

Figure 1. (a) SEM image of PFH@PLGA/Fe_3O_4 nanocapsules (magnification, 3000×; scale bar, 1 μm). TEM images of (b) PLGA nanocapsules, (c) Fe_3O_4@PLGA nanocapsules, and (d) PFH@PLGA/Fe_3O_4 nanocapsules. The dark mass in the center of the spheres is the PFH inner core (d, red dotted circle). The white arrow marks large amounts of Fe_3O_4 nanoparticles embedded in the spherical shell in the form of black particles (c, d). (b–d: Magnification, 93 000×; scale bar, 100 nm.) (e, f) Size distributions and zeta potential of PFH@PLGA/Fe_3O_4 nanocapsules.

To study the effect of irradiation time on cell apoptosis, we cultured another eight groups of cells in 10 cm culture dishes. Groups I and II were control groups without irradiation. In groups III–VIII, the dishes were grouped according to different infrared irradiation times (III, 2 min; IV, 4 min; V, 6 min; VI, 8 min; VII, 10 min; and VIII, 12 min). First, 0.2 mL of PFH@PLGA/Fe_3O_4 nanocapsules (320 μg/mL) was added to the culture media of groups II–VIII and incubated for 3 h. Then, groups III–VIII were irradiated for a certain time at the same distance of 15 cm. An infrared thermometer (Fluke Ti32; USA) was used to monitor the temperature of the culture media per minute when the dishes were irradiated with infrared radiation.

2.7.3. Cell Apoptosis Induced by NIR with Different Types of Nanocapsules. We performed another cell experiment to observe the photothermal effects of different types of nanocapsules on the cell apoptosis rate. Each dish was assigned randomly into one of six groups, and each group consisted of six samples: (A) blanked control group (without any treatment), (B) PFH@PLGA/Fe_3O_4 without infrared irradiation, (C) pure infrared irradiation, (D) PLGA + infrared irradiation, (E) PFH@PLGA + infrared irradiation, (F) Fe_3O_4@PLGA+ infrared irradiation, and (G) PFH@PLGA/Fe_3O_4 + infrared irradiation. The corresponding nanocapsules (0.2 mL, 320 μg/mL) were added to groups B, D, E, F, and G. After 3 h incubation, groups C-G received the same infrared radiation dose at a distance of 15 cm for 5 min.

The cells were subsequently cultured overnight at 37 °C with 5% CO_2 in culture medium containing 10% FBS and 1% penicillin/streptomycin. The cells were digested with trypsin and centrifuged the next day, and flow cytometry was used to analyze cell apoptosis in each group. TEM was used to study the destruction of the remaining sixth dish of groups A–G.

2.8. NIR-Induced PTT for in Vivo Tumor Ablation. One month after inoculation, nude mice bearing xenograft tumors were examined to verify the photothermal effect on tumor ablation induced by NIR irradiation. Thirty-six nude mice bearing xenograft tumors were divided into six groups: (I) untreated group, (II) pure infrared irradiation, (III) PLGA combined with infrared irradiation, (IV) PFH@PLGA combined with infrared irradiation, (V) Fe_3O_4@PLGA combined with infrared irradiation and (VI) PFH@PLGA/Fe_3O_4 combined with infrared irradiation. In groups III–VI, the nude mice received a percutaneous injection of 0.2 mL (320 μg/mL) PLGA, PFH@PLGA, Fe_3O_4@PLGA, or PFH@PLGA/Fe_3O_4 nanocapsule solutions into the site of the tumor and were massaged for 1 min before being subjected to infrared irradiation. The pure infrared irradiation group (II) received infrared irradiation only, and the untreated group (I) received no treatment. All nude mice in groups II–VI were irradiated with infrared radiation at a distance of 15 cm for 12 min. The infrared irradiation was carried out twice.

Twenty-four hours after processing, the nude mice were euthanized and the tumors were excised for histologic analysis. Tumors were fixed in 4% paraformaldehyde overnight, embedded in paraffin, and sectioned for assessing tumor cell proliferation by immunohistochemical staining with antibodies against proliferating cell nuclear antigen (PCNA). We detected apoptosis using the TdT-mediated dUTP nick end labeling (TUNEL assay) method. Paraffin tissue sections were examined by Prussian blue staining to determine the presence of Fe_3O_4 nanocapsules in tissue sections. Moreover, histopathological analysis was performed on paraffin tissues sections stained with hematoxylin and eosin stains. The slides were then observed under a light microscope to compare the difference between the experimental group and control groups. Another 1 mm^3 tissue section was sampled by glutaraldehyde to observe the ultrastructural changes of the targeted tissue under TEM.

3. RESULTS AND DISCUSSION

3.1. Structural Characterization of PFH@PLGA/Fe_3O_4 Nanocapsules. SEM images of the nanocapsules (Figure 1a) show that they have a smooth and uniform spherical morphology. Figure1b–d depict typical TEM images of PLGA, Fe_3O_4@PLGA, and PFH@PLGA/Fe_3O_4 nanocapsules. The presence of Fe_3O_4 nanoparticles in the nanocapsule shells is depicted in Figures 1c, d, which show a large number of black particles embedded in the spherical shell (white arrows). Figure 1d depicts a dark mass in the center of the spheres (red dotted circle) in addition to the black particles, revealing the presence of liquid PFH. Pure PLGA nanocapsules in the absence of Fe_3O_4 and PFH exhibited a blank structure with nothing in the center of the spherical shell (Figure 1b). The nanocapsule size distribution was nearly symmetric, as determined by dynamic light scattering (Figure 1e, mean diameter: 347 nm, PDI = 0.102). The prepared nanocapsule surface was negatively

DOI: 10.1021/acsami.5b01873
ACS Appl. Mater. Interfaces 2015, 7, 14231–14242

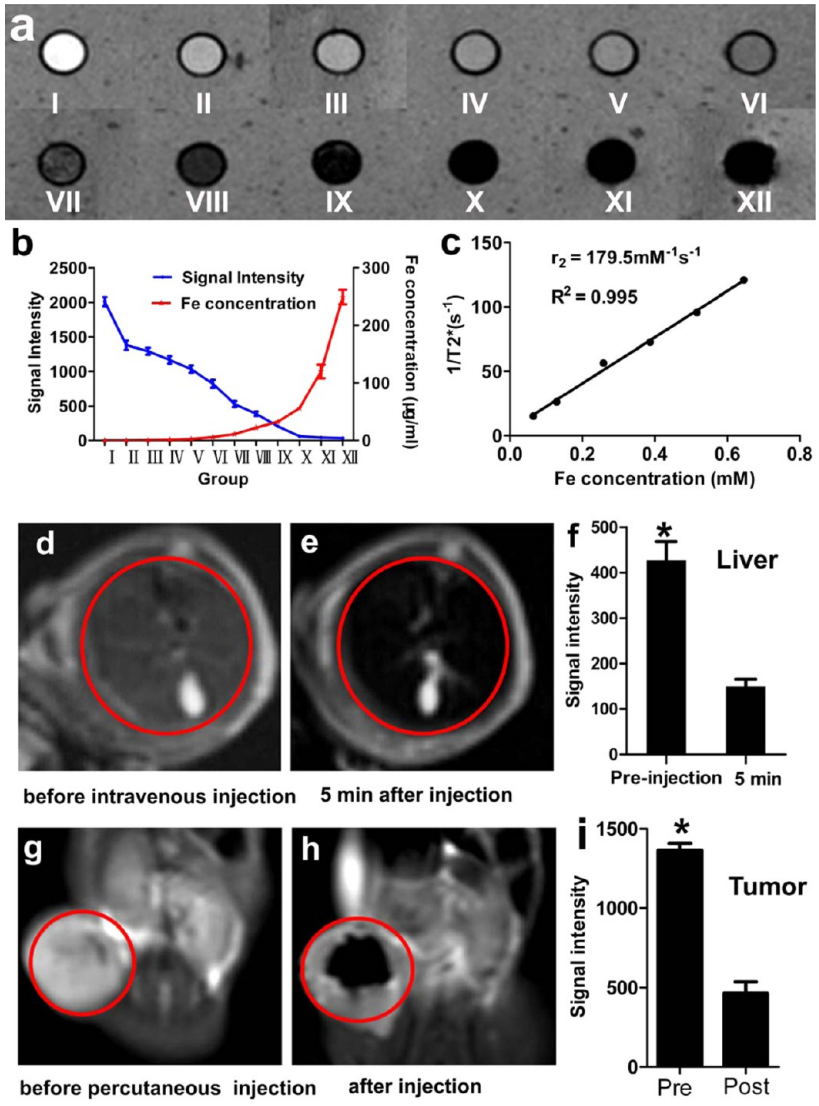

Figure 2. (a) In vitro T2*-weighted MR image. I, Deionized water; II, pure nanoparticles; III–XII, PFH@PLGA/Fe_3O_4 nanocapsules with different Fe_3O_4 concentrations. (b) Different iron concentrations (red curve) and MR signal intensities of the PFH@PLGA/Fe_3O_4 nanocapsules (blue curve) in groups I–XII. (c) T2* relaxation rates (1/T2*(s^{-1})) of PFH@PLGA/Fe_3O_4 emulsion at different iron concentrations. (d, e) In vivo liver MR image of nude mice (areas in red circle) before and 5 min after intravenous injection with PFH@PLGA/Fe_3O_4 nanocapsules. (g, h) In vivo tumor MR image of nude mice (areas in red circle) before and after percutaneous local injection with PFH@PLGA/Fe_3O_4 nanocapsules. (f, i) Signal intensity of MR contrast-enhanced scan images is significantly lower than that of the plain scan images. The difference was statistically significant (*p < 0.05).

charged (Figure 1f, zeta potential: −25.2 mV). The corresponding concentrations of Fe_3O_4 nanoparticles encapsulated in the PFH@PLGA/Fe_3O_4 nanocapsules with different iron concentrations (2.5, 5, 10, 20, 40, 80, 160, 320, 640, and 1280 μg/mL), as measured by atomic absorption spectrometry, were 0.64 ± 0.09, 1.39 ± 0.09, 2.66 ± 0.30, 5.378 ± 0.68, 10.76 ± 1.26, 21.49 ± 0.75, 30.0 ± 1.27, 55.55 ± 1.24, 117.11 ± 2.10, and 247.30 ± 1.68 μg/mL, respectively. PFH@PLGA/Fe_3O_4 nanocapsules exhibit a broad absorption ranging from UV to NIR region which was shown in the absorption spectra (see the Supporting Information, Figure S1).

3.2. In Vitro and in Vivo MRI Assessment of PFH@PLGA/Fe_3O_4 Nanocapsules. In vitro MRI experiments, as shown in the T2* phantom images (Figure 2a), revealed that PFH@PLGA/Fe_3O_4 nanocapsules negatively enhanced the T2*-weighted MR images. The corresponding amount of Fe_3O_4 nanoparticles encapsulated in the nanocapsules is represented by the red curve (Figure 2b). The MRI signal intensity of different groups (I-XII) is shown as the blue curve (Figure 2b). The corresponding amounts of Fe_3O_4 and the mean MRI signal intensity of deionized water, pure nanocapsules, and the PFH@PLGA/Fe_3O_4 nanocapsules with different iron concentrations were acquired (see th eSupporting Information, Table S1). Figure 2c showed the T2 relaxation rates (1/T2*) of PFH@PLGA/Fe_3O_4 solutions at different iron concentrations. The MRI signal intensity decreased with increasing iron concentration, which demonstrated that PFH@PLGA/Fe_3O_4 nanocapsules produced the magnetic resonance contrast on a transverse photon relaxation-time-weighted sequence.

We further assessed the ability of PFH@PLGA/Fe_3O_4 nanocapsules as contrast agents for in vivo MR imaging. As shown in Figures 2d-e, g-h the PFH@PLGA/Fe_3O_4 nanocapsules generated significantly negative contrast enhancement

DOI: 10.1021/acsami.5b01873
ACS Appl. Mater. Interfaces 2015, 7, 14231–14242

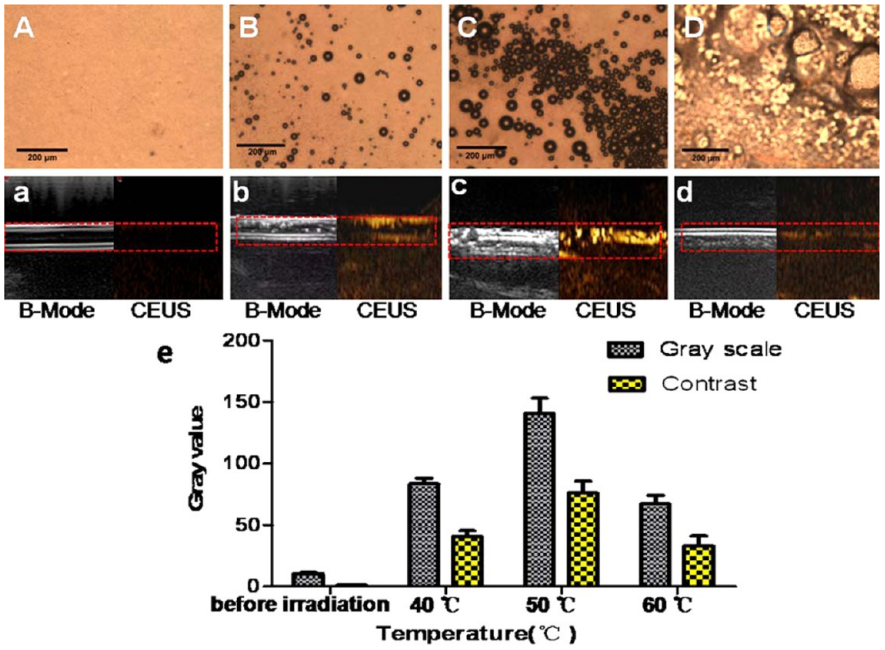

Figure 3. Different optical microscopic images of the PFH@PLGA/Fe_3O_4 nanocapsule phase transition at different temperatures and under NIR irradiation: (A) before infrared irradiation; (B) after more and more small microbubbles were generated at 40 °C; (C) after the quantity of microbubbles reached a maximum at 50 °C; (D) after most microbubbles burst and disappeared at 60 °C. A–D: Magnification, 100×; scale bar, 200 nm) B-mode (left) and contrast-enhanced ultrasound CEUS (right) image of PFH@PLGA/Fe_3O_4 nanocapsules (a) before infrared irradiation and when the temperature reached (b) 40, (c) 50, and (d) 60 °C under irradiation (red dotted line). (e) Acoustic intensity values of PFH@PLGA/Fe_3O_4 nanocapsules changed along with the change in temperature under irradiation.

in liver and tumor tissues by shortening the transverse relaxation of surrounding protons. Compared with the previous image, the liver parenchyma (area in red circle) signal intensity was significantly decreased 5 min after tail intravenous injection with PFH@PLGA/Fe_3O_4 nanocapsules (Figure 2d-, e). T2*-signal intensity in liver decreased by 65.1% 5 min after tail intravenous injection (Figure 2f). Obvious darkening effects were also observed at the tumor site after percutaneous local injection with MR signals decreased by 65.9% (Figure 2i). The presence of Fe_3O_4 nanoparticles in PFH@PLGA/Fe_3O_4 nanocapsules could endow the composite nanocapsules with the property of contrast-enhanced T2*/T2-weighted MR imaging. The in vitro and in vivo results demonstrated that PFH@PLGA/Fe_3O_4 nanocapsules could be used as a contrast agent for MR imaging.

3.3. NIR-Induced Phase Transition for US Imaging with PFH@PLGA/Fe_3O_4 Nanocapsules. Before NIR irradiation, no phase transition occurred in the PFH@PLGA/Fe_3O_4 nanocapsules; therefore, no gas bubbles were observed under the microscope (Figure 3A). The nanocapsules were gradually converted into microbubbles after NIR irradiation (Figure 3B). As the irradiation time was increased, more and more microbubbles were generated. When the temperature reached 50 °C, numerous microbubbles were apparent (Figure 3C). However, these microbubbles started to collapse and disappeared as the temperature continued to increase. Almost all gas bubbles were destroyed at the higher temperature (60 °C, Figure 3D). From these observations of the phase transition from nanocapsules to microbubbles, we determined that 50 °C may be the optimal temperature for phase transition. The nanocapsules in the rubber tube exhibited no echo or enhancement in B-mode and CEUS before irradiation (Figure 3a). After irradiation, more and more gas bubbles appeared as the temperature was increased. The B-mode and CEUS images showed obviously increased echogenicity and contrast enhancement at 50 °C (Figure 3c). Comparatively, the contrast-enhanced ultrasound imaging was very weak at 40 and 60 °C because of the absence of sufficient microbubbles (Figures 3b, d). The histogram (Figure 3e) shows that the acoustic intensity value changed at different temperatures after irradiation. The ultrasonography findings were consistent with microbubble production.

In the in vivo US imaging experiment, the monitor showed that the normal mouse body temperature was approximately 31 °C and that the tumor tissue temperature began to increase as the irradiation time increased. Figure 4A and the Supporting Information, Table S2, show the temperature changes in nude mouse tumor tissues in different groups at a fixed distance of 15 cm. A remarkable temperature increase was observed in the PFH@PLGA/Fe_3O_4 and Fe_3O_4@PLGA nanoparticle groups after 12 min of irradiation, but only a slight temperature increase (approximately 10 °C) was observed in the PFH@PLGA and pure PLGA groups compared with the other groups. Four ultrasound images from groups I–IV were recorded before the NIR irradiation (Figure 4a1–d1), after irradiation for 2 min (Figure 4a2–d2), 5 min (Figure 4a3–d3) and 12 min (Figure 4a4–d4), respectively. The red dotted circles indicate the tumor locations. No contrast-enhanced ultrasound imaging was observed in the control group tumors (I - III) before (Figure 4a1-c1) and after NIR irradiation for 2 min (Figure 4a2–c2), 5 min (Figure 4a3–c3), and 12 min (Figure 4a4–c4) under the contrast mode. Experimental group IV (PFH@PLGA/Fe_3O_4) exhibited obvious contrast-enhanced ultrasound imaging under the contrast mode after infrared irradiation for 2 min (Figure 4d2), and this contrast enhancement was more intense after 5 min of irradiation (Figure 4d3). However, the contrast-enhanced imaging disappeared gradually after a few minutes and became very weak after 12 min of irradiation

DOI: 10.1021/acsami.5b01873
ACS Appl. Mater. Interfaces 2015, 7, 14231–14242

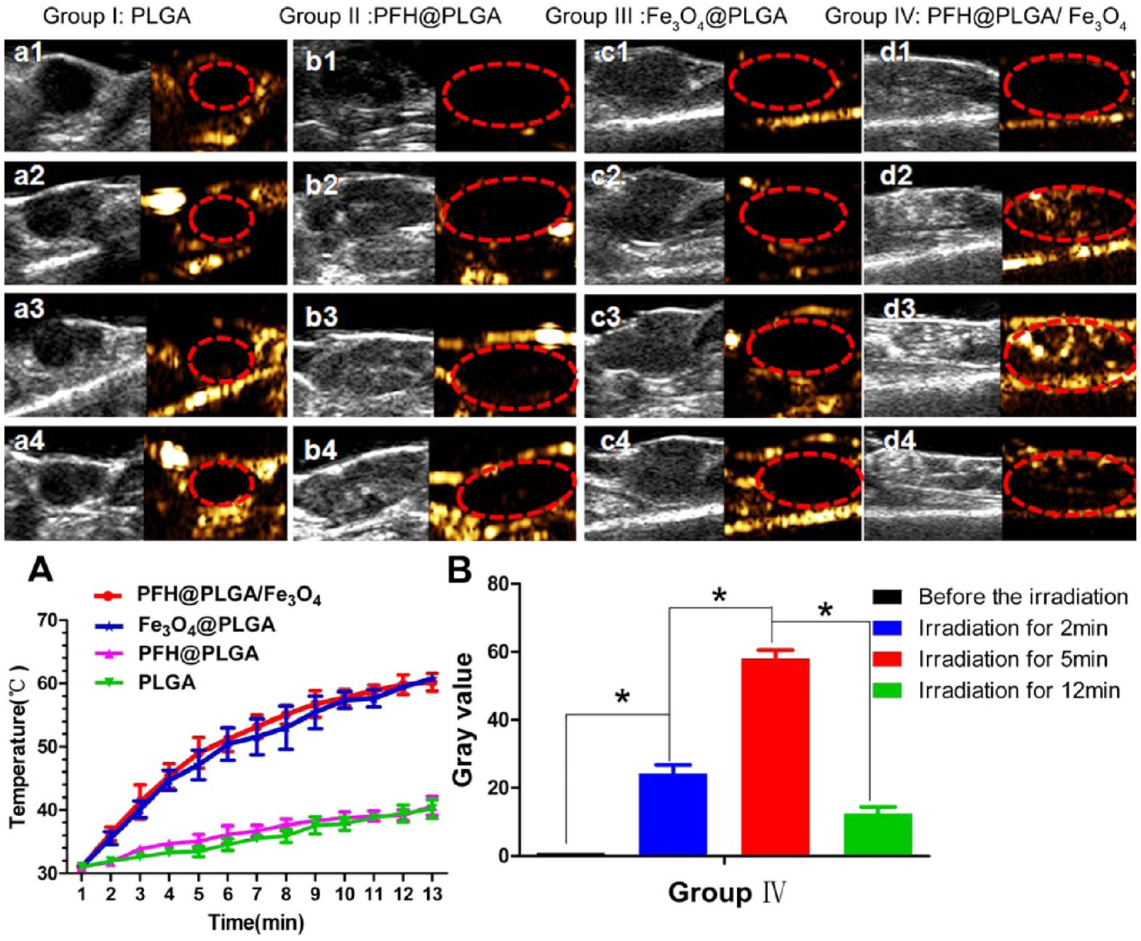

Figure 4. (A) Temperatures of four groups injected with different nanocapsules increased with increasing irradiation time. Four ultrasound images of groups I–IV (a1–d1) before irradiation and after irradiation for (a2–d2) 2 min, (a3–d3) 5 min, and (a4–d4) 12 min (B-mode (left) and contrast-enhanced ultrasound CEUS (right)). The red dotted circles indicate tumor location. (B) Bray value of each ultrasound image in group IV (PFH@PLGA/Fe_3O_4 nanocapsules) (*$p < 0.05$). An asterisk (*) indicates significant difference between any two images (d1–d4) in the gray value of group IV.

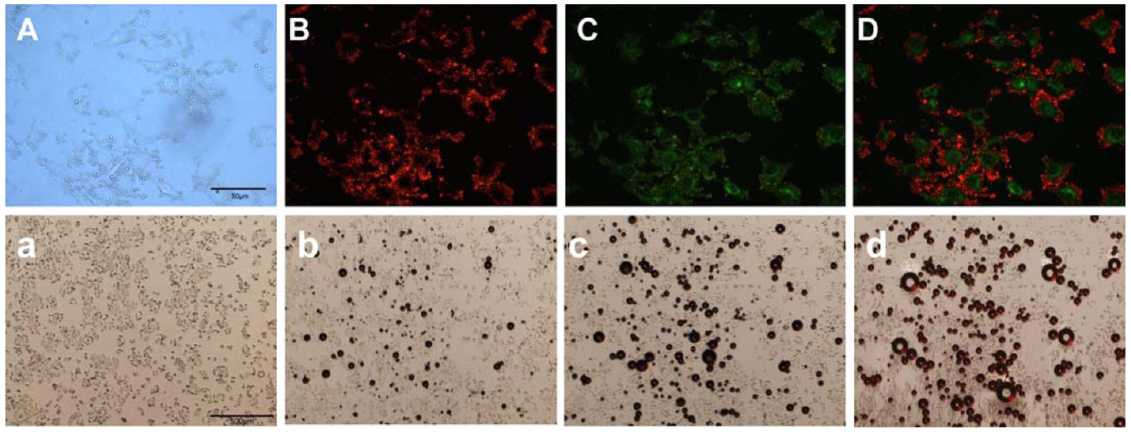

Figure 5. (A–D) Numerous red particles were observed around or inside the dyed green cells (Magnification, 400×; scale bar, 50 μm). (a–d) Intracellular nanocapsule phase-transition process upon infrared irradiation (Magnification, 40×; scale bar, 500 μm).

(Figure 4d4). The gray value of each ultrasound image in group IV was measured using the Integrated Performance Primitives software library, and we accordingly created a histogram to directly embody the gray value change (Figure 4B). A significant difference was observed between any two images in the gray value of group IV (*$p < 0.05$). The CEUS gray value was the highest when the temperature reached 50 °C after irradiation for 5 min.

We speculated that the Fe_3O_4 nanoparticles wrapped in the nanocapsules absorbed the infrared rays and produced strong heating effects instantaneously, which caused the internal temperature in nanocapsules was much higher than surround-

DOI: 10.1021/acsami.5b01873
ACS Appl. Mater. Interfaces 2015, 7, 14231–14242

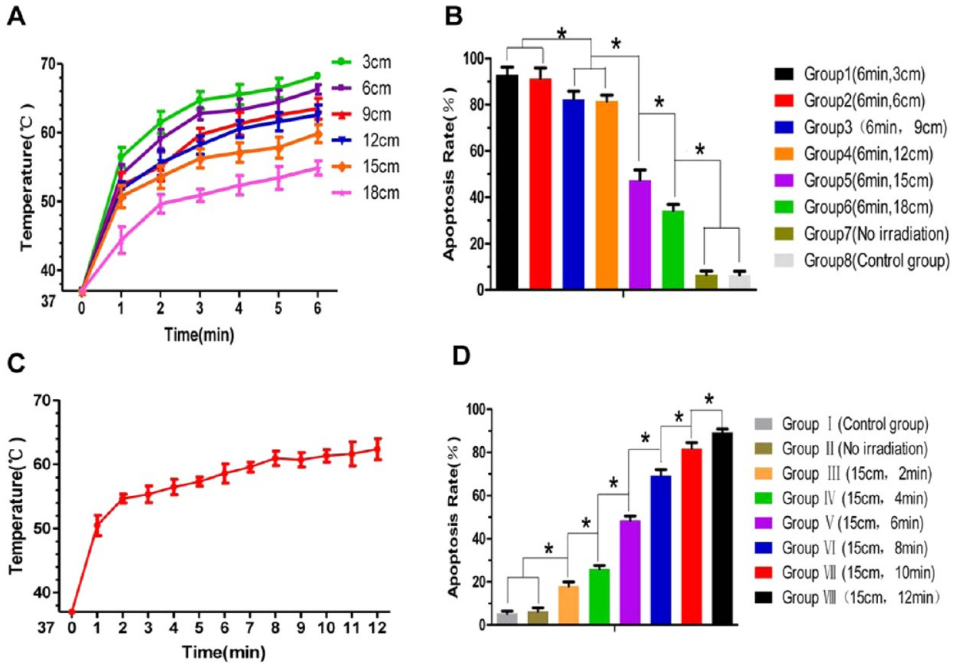

Figure 6. (A) Temperature increased with extended irradiation time (1, 2, 3, 4, 5, and 6 min) and decreased with increased irradiation distance (3, 6, 9, 12, 15, and 18 cm). (B) Cell apoptosis rates of groups 1−8. The cell apoptosis rates decreased with increasing infrared irradiation distance (*p < 0.05). (C) Temperature increased with extended irradiation time (from 1 to 12 min) at a fixed distance of 15 cm. (D) Cell apoptosis rates of groups I-XII (*p < 0.05). An asterisk (*) represents significant differences in cell apoptosis rates in different groups at p < 0.05.

ing temperature and the boiling point of liquid PFH (≈ 56 °C). It was sufficient to induce the liquid−gas phase transition. Large numbers of microbubbles were generated by the PFH phase transition in the nanocapsules after infrared irradiation. This microbubble generation further induced the contrast enhancement of the tumor ultrasound image in nude mice. The contrast-enhanced ultrasound imaging was most intense when irradiation time was 5 min and the temperature was approximately 50 °C. The contrast enhancement ultrasound imaging intensity gradually decreased along with microbubble destruction when the tumor was irradiated for a longer time, and its intensity was enhanced when the microbubbles were generated again during the second irradiation. The PFH@PLGA nanocapsules did not absorb infrared radiation and could not generate as much heat as the PFH@PLGA/Fe_3O_4 nanocapsules. Thus, no microbubbles were generated and the ultrasound image was not enhanced.

3.4. NIR-Induced Photothermal Effect for Cell Ablation in Vitro. *3.4.1. NIR-Induced Phase Transition with PFH@PLGA/Fe_3O_4 Nanocapsules in Vitro.* Figure 5A shows a bright-field optical microscope image of the PFH@PLGA/Fe_3O_4 nanocapsules and cells. Under a fluorescence microscope, the nanocapsules labeled by Dil emitted bright red fluorescence (Figure 5B) and the cells emitted bright green light (Figure 5C). These images were superimposed and transformed into the third image. Numerous red particles were observed around or inside the dyed green cells, indicating that many PFH@PLGA/Fe_3O_4 nanocapsules adhered to the cytomembrane and that some nanocapsules were engulfed by the cells (Figure 5D).

As observed at 40× magnification, a large number of small microbubbles emerged around the cells and the intracellular space and the number of these microbubbles increased as the irradiation time was extended (Figures 5a−d). This phenomenon demonstrates that the nanocapsule phase transition can feasibly occur in cells and offers the potential for further diagnosis and agent-assisted therapy.

3.4.2. Cell Apoptosis Induced by NIR with PFH@PLGA/Fe_3O_4 Nanocapsules in Vitro. Using the results from groups 1−8, we constructed a chart indicating that the temperature increased with increasing irradiation time (1, 2, 3, 4, 5, and 6 min) at a fixed distance and decreased with increasing irradiation distance (3, 6, 9, 12, 15, and 18 cm) at a fixed irradiation time (see the Supporting Information, Table S3). From the line graph shown in Figure 6A, we concluded that the temperature increased with increasing irradiation time at the fixed distance and decreased with increasing distance after being irradiated for the same time. The cell apoptosis rate of each group was calculated by taking an average of the data from the flow cytometry experiments. A histogram depicting the rate of cell apoptosis was plotted to compare the apoptosis in each group (Figure 6B). We noted that the cell apoptosis rate decreased as the irradiation distance increased from group 1 to 6, which is in accordance with the temperature variation. The cell apoptosis rates in groups 1−6 were significantly higher than those in the control groups 7 and 8 (*p < 0.05), and no significant difference was observed in the cell apoptosis rates between group 7 and 8 (p > 0.05). Because of the relationship between temperature and irradiation distance, we chose 15 cm as the optimal irradiation distance for the apoptosis experiment. Because the optimum temperature fell within the temperature from 50.3 ± 0.28 °C to 59.24 ± 0.71 °C at an irradiation distance of 15 cm, it facilitated the phase transformation and led to better echo signals and contrast enhancement for the images.

A histogram was drawn to describe the variation in cell apoptosis along with the irradiation time at a fixed irradiation distance of 15 cm (Figure 6D). From the histogram, we concluded that the cell apoptosis rate from group III to group VIII increased with increasing irradiation time. This conclusion

DOI: 10.1021/acsami.5b01873
ACS Appl. Mater. Interfaces 2015, 7, 14231−14242

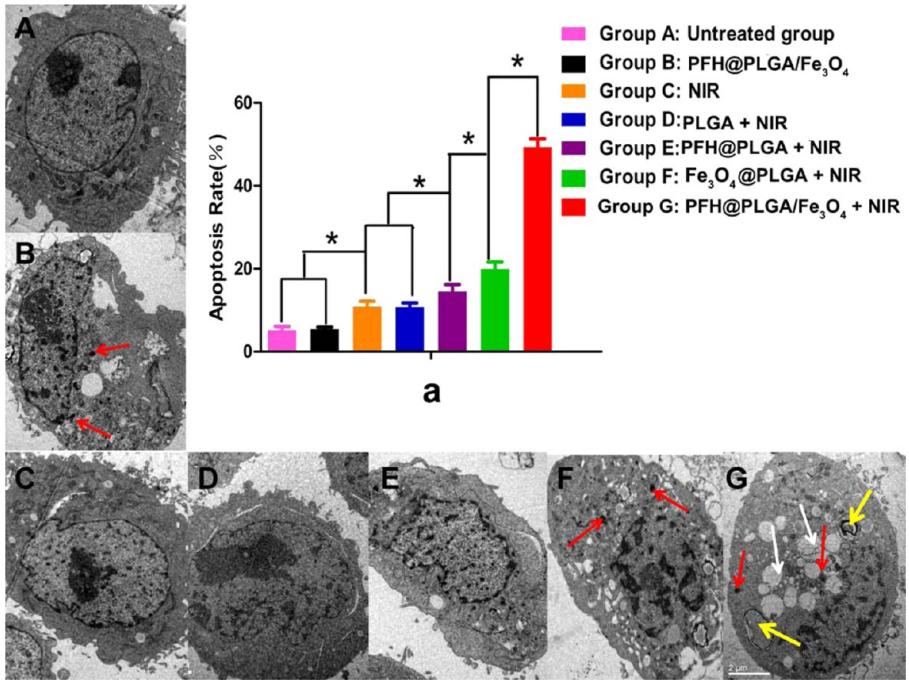

Figure 7. (a) Cell apoptosis rates of groups A–G (*$p < 0.05$). An asterisk (*) represents significant differences in cell apoptosis rates in different groups at $p < 0.05$. (A–G) TEM analysis of cells in groups A–G. As shown in G, many vacuoles (white arrows) and myelins (yellow arrows) appeared in the cells. Fe_3O_4 nanoparticles (red arrows) were observed to be deposited along the cytoplasmic location (B, F, 7). High electronic density was not detectable in A, C, D, and E. (A–G: Magnification, 10 000×; scale bar, 2 μm.).

is consistent with the time-dependent temperature variation (Figure 6C). The apoptosis rates of the experimental groups (III–VIII) were significantly higher than that of the control groups I and II (*$p < 0.05$). No significant difference in apoptosis rate was observed between groups I and II ($p > 0.05$). All the charts show that the temperature increased as the irradiation time was extended and decreased as the irradiation distance was increased. The apoptosis rate was thus related to the irradiation temperature. Excessively high temperatures would burn the skin of the nude mice and inflict damage to normal tissues, whereas excessively low temperatures would not sufficiently kill all the tumor cells. From the results of these cell apoptosis experiments, we chose an optimal irradiation distance of 15 cm and optimum irradiation time of 5 min for further tumor imaging and treatment experiments. The temperature for the PTT was higher than 50 °C, the possible side effects related to the high temperature should be concerned in future clinical translation. For the local injection method, real time ultrasound should be employed for the accurate injection of the PFH@PLGA/Fe_3O_4 nanoparticles in order to avoid the potential damage to the surrounding tissue. For the i.v. injection method, it is very important to improve the accumulation of the nanoparticles to the tumor site and decrease the nonspecific distribution in normal tissues.

3.4.3. Different Cell Apoptosis Rates Induced by NIR with Different Types of Nanocapsules. We plotted a histogram to compare the different apoptosis rates among groups (A–G) (Figure 7a). The cell apoptosis rate gradually increased from group A to group G. The cell apoptosis rate of group G (PFH@PLGA/Fe_3O_4 + infrared irradiation) was significantly greater than that of any other group (*$p < 0.05$). The cell apoptosis rates of groups C–G with infrared irradiation were higher than those of groups A and B (*$p < 0.05$).

The extent of cell necrosis was consistent with the cell apoptosis results, as visualized by TEM (Figures 7A–G). In the blank control group, the chromatin condensed in a few cells and the cell morphology was normal (Figure 7A). In groups B–D, the general cell structure was still present, the cell and nuclear membranes were intact, and the mitochondria and endoplasmic reticulum were slightly distended (Figures 7B–D). Comparatively, in groups E and F, the cell structures were not clear and most cell and nuclear membranes were interrupted or were undefined, with dilated endoplasmic reticulum and swollen mitochondria (Figure 7E, F). In group G, obvious degeneration of vacuolation (white arrows) and numerous vacuoles and myelin figures (yellow arrows) were observed. In addition, organelles disappeared, some organelles were lysed, cell necrosis was much more evident, and nuclear membranes disintegrated. In groups B, F, and G, which were treated with Fe_3O_4@PLGA or PFH@PLGA/Fe_3O_4 nanocapsules, Fe_3O_4 nanoparticles were observed to be regularly deposited along the cytoplasm around the nuclear membranes in residual tumor cells (Figures 7B, F, and G), whereas no Fe_3O_4 nanoparticles were observed in the cells of other groups. This result indicated that the composite microcapsules were taken up by cells.

3.5. NIR-Induced PTT for Tumor Ablation in Vivo. A large number of small bubbles were observed on the surface of tumors excised from the nude mice in group VI (PFH@PLGA/Fe_3O_4). Similar phenomena were not observed on the tumors excised from the nude mice of the other groups, which further confirmed the occurrence of a liquid–gas phase transition. Upon microscopic examination, the tumor tissue in the mice of control group I (without receiving agents and infrared irradiation) and group II (receiving infrared irradiation only) showed a normal morphology after HE staining (Figure 8a1, a2). In the case of group VI, the tumor cells were arranged in

DOI: 10.1021/acsami.5b01873
ACS Appl. Mater. Interfaces 2015, 7, 14231–14242

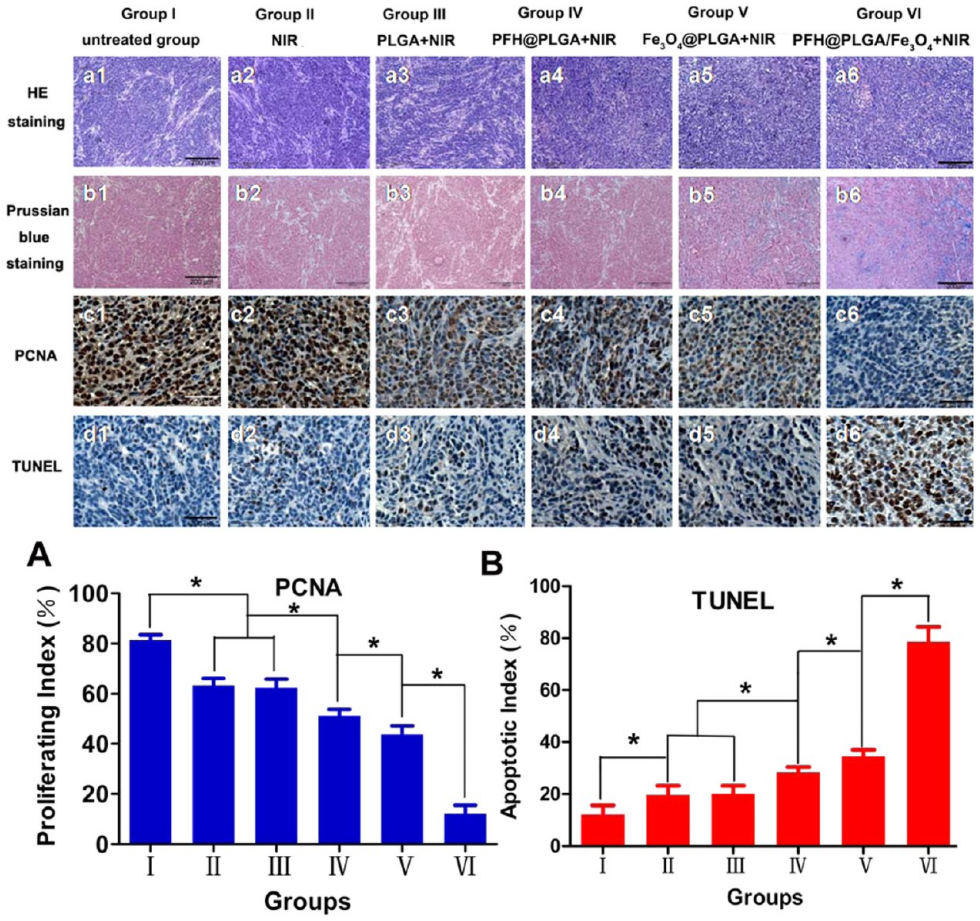

Figure 8. Pathological examination results of nude tumor tissue in groups I–VI. Microscope images of (a1–a6) HE staining, (b1–b6) Prussian blue staining, (c1–c6) PCNA, and (d1–d6) TUNEL staining of tumor tissues. a1–a6, b1–b6: Magnification, 100×; scale bar, 200 μm. c1–c6, d1–d6: Magnification, 400×; scale bar, 50 μm. (A, B) Proliferating index and the apoptosis index of tumor tissues in groups I–VI ($^*p < 0.05$). An asterisk (*) indicates significant difference in proliferating index and the apoptosis index in different groups.

nests and the tumor tissue exhibited distinct and widespread coagulative necrosis (Figure 8a6). Severe damage was evident, including lysed cell membranes and nuclear fragmentation. In the other three groups (III, IV, and V), various extents of injury without qualitative differences were observed (Figures 8a3–a5). The tumor tissue damage in the three groups was slighter and weaker compared with group VI.

To further validate the existence of PFH@PLGA/Fe_3O_4 nanocapsules in tumor tissues, we obtained microscope images of tissue slices stained with Prussian blue; these images revealed that iron was present in the tumor tissues from groups V and VI (Figure 8b5, b6), whereas blue staining was not observed in the tumor tissues from groups I–IV (Figure 8b1–b4). Proliferating cell nuclear antigen protein and apoptosis expression were semiquantitatively obtained by counting the number of cells stained positively from 6 randomly selected high-power fields (400× magnification). The proliferating index (PI) and the apoptotic index (AI), expressed as the ratio of positively stained tumor cells to all cells, and were determined by reading 6 random areas in high-power fields. The PCNA expression manifested as brown granules in cell nuclei, and its expression was observed in all six groups (Figure 8c1–c6). Figure 8A shows the PI of tumor tissues in groups I–VI. The results showed that the PI for the tumors in group VI was significantly lower than those for the tumors in any other groups ($^*p < 0.05$, Figure 8A). Significant PI differences were observed between any two groups, besides groups II and III ($^*p < 0.05$), and the tumor tissue expression of group I was the highest among all six groups ($^*p < 0.05$).

Cell apoptosis in tissue sections was assessed using a TUNEL assay. Apoptotic cells showed brown stains in their nuclei. Similar to the proliferation assay, apoptotic cells were observed in all six groups (Figure 8d1–d6). As shown in Figure 8B, the AI for group VI tumors was far higher than in the other groups ($^*p < 0.05$). Significant AI differences were observed between any two groups, besides group II and group III ($^*p < 0.05$). The tumor tissue expression in group I was the lowest among all six groups ($^*p < 0.05$).

In blank control group I, the cell structures were normal and clear, the cell and nuclear membranes were intact, and the mitochondria and endoplasmic reticula were slightly distended (see the Supporting Information, Figure S2a). In addition to the evident coagulative necrosis in group VI, most cell membranes were ruptured, nuclear membranes were disintegrated (karyorrhexis), some cytoplasm was dissolved, and organelles had disappeared, which was consistent with the HE staining results, as visualized by TEM (see the Supporting Information, Figure S2b).

Two main factors may be involved that illustrate the synergistic effect of the PFH@PLGA/Fe_3O_4 nanocapsules for infrared irradiation. First, the metal oxide (Fe_3O_4) present in the composite nanocapsules absorbed the infrared rays and

DOI: 10.1021/acsami.5b01873
ACS Appl. Mater. Interfaces 2015, 7, 14231–14242

generated thermal effects in tissue. Second, the increasing tissue temperature induced the liquid−gas phase transition. Furthermore, microbubble generation and bursting enhanced the tumor ablation effect. In conclusion, the thermal effects of infrared irradiation and thermoelastic expansion of the nanocapsule phase transition caused a synergistic effect that induced coagulative necrosis and damage in tumors.

4. CONCLUSION

In this study, we synthesized multifunctional PFH@PLGA/Fe_3O_4 nanocapsules, employed NIR light for PTT therapy and reported a novel NIR radiation droplet vaporization (NIRDV) method for multimodal molecular imaging and cancer hyperthermia treatment. We developed the NIRDV method to induce PFH droplet encapsulated nanocapsule vaporization using the portable infrared lamp. Fe_3O_4 nanoparticles of various shapes have been found to exhibit strong photothermal effects, induced by red and NIR laser irradiation.[11] Chen et al. synthesized highly crystallized iron oxide nanoparticles (HCIONPs) and found that the preferred lane orientation may contribute to the effective absorption of infrared light for HCIONPs.[33] In this study, the photothermal generation might be based on high crystallite structure of magnetic Fe_3O_4 nanoparticles. After exposure to infrared radiation, the magnetic Fe_3O_4 nanoparticles absorbed the infrared light and transformed light energy to heat energy, which made the inner temperature of PFH@PLGA/Fe_3O_4 nanocapsules instantaneously increase much higher than surrounding temperature and the vaporization temperature of liquid PFH, thus facilitated the vaporization of the inner liquid PFH. The thermal effect of infrared irradiation and the thermoelastic expansion effect of nanocapsule phase transitioning caused a synergistic effect that induced coagulative necrosis and damage in tumors. Simultaneously, the presence of Fe_3O_4 nanoparticles and the vaporization gas bubbles made the PFH@PLGA/Fe_3O_4 nanocapsules a nice contrast agent for MR and ultrasound imaging. Our research confirmed that the nanocapsules are feasible as both synergistic agents to strengthen tumor ablation efficiency and dual-mode contrast agents to provide significant contrast enhancement for MR and ultrasound imaging.

■ ASSOCIATED CONTENT

Supporting Information

The corresponding amount of Fe_3O_4 and mean signal intensity of MRI for the PFH@PLGA/Fe_3O_4 nanocapsules with different iron concentration, UV−vis−NIR absorbance spectra of PFH@PLGA/Fe_3O_4 solutions, different groups of nude mouse tumor tissue temperature changes with the extended irradiation time, relationship between temperature and irradiation time or distance, and TEM analysis of tumor tissues after photothermal therapy. The Supporting Information is available free of charge on the ACS Publications website at DOI: 10.1021/acsami.5b01873.

■ AUTHOR INFORMATION

Corresponding Authors

*E-mail: cqlipan@163.com.
*E-mail: zhengyuanyi@gmail.com.

Notes

The authors declare no competing financial interest.

■ ACKNOWLEDGMENTS

This work was financially supported by the National Natural Science Foundation of China (Grants 81227801, 81270021, 81371578), National Distinguished Young Scholars (Grant 81425014), Chongqing Science Fund for Distinguished Young Scholars (cstc2013jcyjjq10004), and the Natural Science Foundation of Chongqing (cstc2013jcyjA10002).

■ REFERENCES

(1) Shen, S.; Kong, F.; Guo, X.; Wu, L.; Shen, H.; Xie, M.; Wang, X.; Jin, Y.; Ge, Y. Cmcts Stabilized Fe_3O_4 Particles with Extremely Low Toxicity as Highly Efficient near-Infrared Photothermal Agents for in Vivo Tumor Ablation. *Nanoscale* **2013**, *5*, 8056−8066.
(2) Sharma, P.; Brown, S. C.; Singh, A.; Iwakuma, N.; Pyrgiotakis, G.; Krishna, V.; Knapik, J. A.; Barr, K.; Moudgil, B. M.; Grobmyer, S. R. Near-Infrared Absorbing and Luminescent Gold Speckled Silica Nanoparticles for Photothermal Therapy. *J. Mater. Chem.* **2010**, *20*, 5182.
(3) Cheng, L.; Yang, K.; Li, Y.; Zeng, X.; Shao, M.; Lee, S. T.; Liu, Z. Multifunctional Nanoparticles for Upconversion Luminescence/Mr Multimodal Imaging and Magnetically Targeted Photothermal Therapy. *Biomaterials* **2012**, *33*, 2215−2222.
(4) Yang, K.; Hu, L.; Ma, X.; Ye, S.; Cheng, L.; Shi, X.; Li, C.; Li, Y.; Liu, Z. Multimodal Imaging Guided Photothermal Therapy Using Functionalized Graphene Nanosheets Anchored with Magnetic Nanoparticles. *Adv. Mater.* **2012**, *24*, 1868−1872.
(5) Strohm, E.; Rui, M.; Gorelikov, I.; Matsuura, N.; Kolios, M. Vaporization of Perfluorocarbon Droplets Using Optical Irradiation. *Biomed. Opt. Express* **2011**, *2*, 1432−1442.
(6) Dong, W.; Li, Y.; Niu, D.; Ma, Z.; Gu, J.; Chen, Y.; Zhao, W.; Liu, X.; Liu, C.; Shi, J. Facile Synthesis of Monodisperse Superparamagnetic Fe_3O_4 Core@Hybrid@Au Shell Nanocomposite for Bimodal Imaging and Photothermal Therapy. *Adv. Mater.* **2011**, *23*, 5392−5397.
(7) Peng, J.; Zhao, L.; Zhu, X.; Sun, Y.; Feng, W.; Gao, Y.; Wang, L.; Li, F. Hollow Silica Nanoparticles Loaded with Hydrophobic Phthalocyanine for near-Infrared Photodynamic and Photothermal Combination Therapy. *Biomaterials* **2013**, *34*, 7905−7912.
(8) Wang, C.; Chen, J.; Talavage, T.; Irudayaraj, J. Gold Nanorod/Fe_3O_4 Nanoparticle "Nano-Pearl-Necklaces" for Simultaneous Targeting, Dual-Mode Imaging, and Photothermal Ablation of Cancer Cells. *Angew. Chem., Int. Ed. Engl.* **2009**, *48*, 2759−2763.
(9) Zhang, Z.; Wang, J.; Nie, X.; Wen, T.; Ji, Y.; Wu, X.; Zhao, Y.; Chen, C. Near Infrared Laser-Induced Targeted Cancer Therapy Using Thermoresponsive Polymer Encapsulated Gold Nanorods. *J. Am. Chem. Soc.* **2014**, *136*, 7317−7326.
(10) Tian, Q.; Hu, J.; Zhu, Y.; Zou, R.; Chen, Z.; Yang, S.; Li, R.; Su, Q.; Han, Y.; Liu, X. Sub-10 Nm Fe_3O_4@$Cu_{2-X}S$ Core-Shell Nanoparticles for Dual-Modal Imaging and Photothermal Therapy. *J. Am. Chem. Soc.* **2013**, *135*, 8571−8577.
(11) Chu, M.; Shao, Y.; Peng, J.; Dai, X.; Li, H.; Wu, Q.; Shi, D. Near-Infrared Laser Light Mediated Cancer Therapy by Photothermal Effect of Fe_3O_4 Magnetic Nanoparticles. *Biomaterials* **2013**, *34*, 4078−4088.
(12) Zhou, Z.; Sun, Y.; Shen, J.; Wei, J.; Yu, C.; Kong, B.; Liu, W.; Yang, H.; Yang, S.; Wang, W. Iron/Iron Oxide Core/Shell Nanoparticles for Magnetic Targeting Mri and near-Infrared Photothermal Therapy. *Biomaterials* **2014**, *35*, 7470−7478.
(13) Shen, S.; Wang, S.; Zheng, R.; Zhu, X.; Jiang, X.; Fu, D.; Yang, W. Magnetic Nanoparticle Clusters for Photothermal Therapy with near-Infrared Irradiation. *Biomaterials* **2015**, *39*, 67−74.
(14) Feng, W.; Zhou, X.; Nie, W.; Chen, L.; Qiu, K.; Zhang, Y.; He, C. Au/Polypyrrole@Fe_3O_4 Nanocomposites for MR/CT Dual-Modal Imaging Guided-Photothermal Therapy: An in Vitro Study. *ACS Appl. Mater. Interfaces* **2015**, *7*, 4354−4367.
(15) Ke, H.; Wang, J.; Tong, S.; Jin, Y.; Wang, S.; Qu, E.; Bao, G.; Dai, Z. Gold Nanoshelled Liquid Perfluorocarbon Magnetic Nanocapsules: A Nanotheranostic Platform for Bimodal Ultrasound/

DOI: 10.1021/acsami.5b01873
ACS Appl. Mater. Interfaces 2015, 7, 14231−14242

Magnetic Resonance Imaging Guided Photothermal Tumor Ablation. *Theranostics* **2013**, *4*, 12−23.
(16) Sun, Y.; Zheng, Y.; Ran, H.; Zhou, Y.; Shen, H.; Chen, Y.; Chen, H.; Krupka, T. M.; Li, A.; Li, P.; Wang, Z.; Wang, Z. Superparamagnetic PLGA-Iron Oxide Microcapsules for Dual-Modality US/MR Imaging and High Intensity Focused Us Breast Cancer Ablation. *Biomaterials* **2012**, *33*, 5854−5864.
(17) Liao, M. Y.; Lai, P. S.; Yu, H. P.; Lin, H. P.; Huang, C. C. Innovative Ligand-Assisted Synthesis of NIR-Activated Iron Oxide for Cancer Theranostics. *Chem. Commun.* **2012**, *48*, 5319−5321.
(18) Zhang, X.; Xu, X.; Li, T.; Lin, M.; Lin, X.; Zhang, H.; Sun, H.; Yang, B. Composite Photothermal Platform of Polypyrrole-Enveloped Fe_3O_4 Nanoparticle Self-Assembled Superstructures. *ACS Appl. Mater. Interfaces* **2014**, *6*, 14552−14561.
(19) Rapoport, N. Y.; Kennedy, A. M.; Shea, J. E.; Scaife, C. L.; Nam, K. H. Controlled and Targeted Tumor Chemotherapy by Ultrasound-Activated Nanoemulsions/Microbubbles. *J. Controlled Release* **2009**, *138*, 268−276.
(20) Rapoport, N. Phase-Shift, Stimuli-Responsive Perfluorocarbon Nanodroplets for Drug Delivery to Cancer. *Wiley Interdiscip. Rev.: Nanomed. Nanobiotechnol.* **2012**, *4*, 492−510.
(21) Li, D. S.; Kripfgans, O. D.; Fabiilli, M. L.; Brian Fowlkes, J.; Bull, J. L. Initial Nucleation Site Formation Due to Acoustic Droplet Vaporization. *Appl. Phys. Lett.* **2014**, *104*, 063703.
(22) Kripfgans, O. D.; Fowlkes, J. B.; Miller, D. L.; Eldevik, O. P.; Carson, P. L. Acoustic Droplet Vaporization for Therapeutic and Diagnostic Applications. *Ultrasound Med. Biol.* **2000**, *26*, 1177−1189.
(23) Wilson, K.; Homan, K.; Emelianov, S. Biomedical Photoacoustics Beyond Thermal Expansion Using Triggered Nanodroplet Vaporization for Contrast-Enhanced Imaging. *Nat. Commun.* **2012**, *3*, 618.
(24) Jian, J.; Liu, C.; Gong, Y.; Su, L.; Zhang, B.; Wang, Z.; Wang, D.; Zhou, Y.; Xu, F.; Li, P.; Zheng, Y.; Song, L.; Zhou, X. India Ink Incorporated Multifunctional Phase-Transition Nanodroplets for Photoacoustic/Ultrasound Dual-Modality Imaging and Photoacoustic Effect Based Tumor Therapy. *Theranostics* **2014**, *4*, 1026−1038.
(25) Qiao, Y.; Zong, Y.; Yin, H.; Chang, N.; Li, Z.; Wan, M. Spatial and Temporal Observation of Phase-Shift Nano-Emulsions Assisted Cavitation and Ablation During Focused Ultrasound Exposure. *Ultrason. Sonochem.* **2014**, *21*, 1745−1751.
(26) Zhou, Y.; Wang, Z.; Chen, Y.; Shen, H.; Luo, Z.; Li, A.; Wang, Q.; Ran, H.; Li, P.; Song, W.; Yang, Z.; Chen, H.; Wang, Z.; Lu, G.; Zheng, Y. Microbubbles from Gas-Generating Perfluorohexane Nanoemulsions for Targeted Temperature-Sensitive Ultrasonography and Synergistic Hifu Ablation of Tumors. *Adv. Mater.* **2013**, *25*, 4123−4130.
(27) Kopechek, J. A.; Park, E. J.; Zhang, Y. Z.; Vykhodtseva, N. I.; McDannold, N. J.; Porter, T. M. Cavitation-Enhanced Mr-Guided Focused Ultrasound Ablation of Rabbit Tumors in Vivo Using Phase Shift Nanoemulsions. *Phys. Med. Biol.* **2014**, *59*, 3465−3481.
(28) Wang, X.; Chen, H.; Chen, Y.; Ma, M.; Zhang, K.; Li, F.; Zheng, Y.; Zeng, D.; Wang, Q.; Shi, J. Perfluorohexane-Encapsulated Mesoporous Silica Nanocapsules as Enhancement Agents for Highly Efficient High Intensity Focused Ultrasound (HIFU). *Adv. Mater.* **2012**, *24*, 785−791.
(29) Sheeran, P. S.; Wong, V. P.; Luois, S.; McFarland, R. J.; Ross, W. D.; Feingold, S.; Matsunaga, T. O.; Dayton, P. A. Decafluorobutane as a Phase-Change Contrast Agent for Low-Energy Extravascular Ultrasonic Imaging. *Ultrasound Med. Biol.* **2011**, *37*, 1518−1530.
(30) Sheeran, P. S.; Luois, S.; Dayton, P. A.; Matsunaga, T. O. Formulation and Acoustic Studies of a New Phase-Shift Agent for Diagnostic and Therapeutic Ultrasound. *Langmuir* **2011**, *27*, 10412−10420.
(31) Reznik, N.; Williams, R.; Burns, P. N. Investigation of Vaporized Submicron Perfluorocarbon Droplets as an Ultrasound Contrast Agent. *Ultrasound Med. Biol.* **2011**, *37*, 1271−1279.
(32) Huang, J.; Xu, J. S.; Xu, R. X. Heat-Sensitive Microbubbles for Intraoperative Assessment of Cancer Ablation Margins. *Biomaterials* **2010**, *31*, 1278−1286.
(33) Chen, H.; Burnett, J.; Zhang, F.; Zhang, J.; Paholak, H.; Sun, D. Highly Crystallized Iron Oxide Nanoparticles as Effective and Biodegradable Mediators for Photothermal Cancer Therapy. *J. Mater. Chem. B* **2014**, *2*, 757−765.

DOI: 10.1021/acsami.5b01873
ACS Appl. Mater. Interfaces 2015, 7, 14231−14242